



Carbon dots enhance the stability of CdS for visible-light-driven overall water splitting



Cheng Zhu, Changan Liu, Yunjie Zhou, Yijun Fu, Sijie Guo, Hao Li, Siqi Zhao, Hui Huang*, Yang Liu*, Zhenhui Kang*

Jiangsu Key Laboratory for Carbon-Based Functional Materials & Devices, Institute of Functional Nano & Soft Materials (FUNSOM), Soochow University, 199 Ren'ai Road, Suzhou, 215123, Jiangsu, PR China

ARTICLE INFO

Article history:

Received 8 February 2017

Received in revised form 11 May 2017

Accepted 18 May 2017

Available online 25 May 2017

Keywords:

CdS-CdS nanocomposite

Photocatalyst

Visible-light water splitting

Catalytic activity and stability

ABSTRACT

Cadmium sulfide (CdS) has long time been one of the most promising inorganic photocatalysts for hydrogen production driven by visible light. However, the photocorrosion of CdS is the most serious problem which constrains its development. Here, we report the design and fabrication of a carbon dots-cadmium sulfide (CDs-CdS) nanocomposite, showing significant photocatalytic water splitting properties with impressive stability without requirement for any sacrificial agents or cocatalysts. The highest hydrogen production rate was obtained for about $2.55 \mu\text{mol h}^{-1}$, with an oxygen evolution rate for about $0.52 \mu\text{mol h}^{-1}$, when the concentration of CDs in the sample is $0.03 \text{ g}_{\text{CDs}}/\text{g}_{\text{catalyst}}$. Even the produced H_2 and O_2 are not equal to the stoichiometric ratio of 2:1 ($\text{H}_2:\text{O}_2$), the CDs-CdS nanocomposite shows greater stability (8-time repetitive catalytic experiments) than the CdS catalysts reported up to now (without sacrificial agents or cocatalysts). It is also inspiring that when we increased the concentration of CDs in the catalysts, the produced H_2 and O_2 were gradually adjusted to meet the stoichiometric ratio of 2:1 in spite of low hydrogen production rate ($0.13 \mu\text{mol h}^{-1}$).

© 2017 Elsevier B.V. All rights reserved.

1. Introduction

Hydrogen is now considered as one of the most promising and environmentally friendly energy. Transformation of solar energy to hydrogen (H_2) via highly effective photocatalyst has been considered a promising strategy to produce clean energy and chemical fuels to mitigate energy problems [1–5]. Semiconductor materials with adjustable band gap and wide wavelength response are excellent candidates as photocatalysts for highly efficient solar water splitting, hence has been triggering extensive interest since 1972, when the first work of hydrogen production based on TiO_2 photo-electrochemical water decomposition was reported by Fujishima and Honda [6–9]. Since then, numerous semiconductor materials have been successfully fabricated and developed as efficient photocatalysts to harvest solar energy for photocatalytic water splitting [10–13].

CdS is one of the most promising candidate for hydrogen evolution research in the past years due to its great visible light response,

narrow band gap, excellent transport properties, good thermal and chemical stability and controllable size and morphology [14]. CdS has been reported in different forms like nanocrystals [15], nanorods [16], nanowires [17], clusters [18], nanosheets [19], and nanoparticles [20] etc. via different synthesis process, which acts as a powerful light harvester in photocatalytic applications [21–23]. The different morphologies of CdS make controllable optical band gap, which influence the band gap structure and electron transfer processes, thus determining light-driven hydrogen evolution properties [24]. However, CdS suffers from an inherent photocorrosion which obstructs its development and application [25]. Photocorrosion is an irreversible phenomenon which often takes place on oxygen and sulfur-containing catalysts during the light irradiating process, meaning that, when the samples are irradiated under light, the induced electrons combine with H^+ , while the induced holes (or other active radicals) will combine with the negion part of catalysts (for CdS is S^{2-}) rather than the O^{2-} from water [26–28]. As a result, hydrogen is produced, but oxygen may not release, and the catalysts are corroded and lose activity quickly. Great efforts have been devoted to developing new CdS structures and systems in the application of photocatalysis as well as solving the photocorrosion problem by many researchers, especially those work achieved by K. Domen, and C. Li et al. In general, the most commonly used

* Corresponding authors.

E-mail addresses: hhuang0618@suda.edu.cn (H. Huang), yangl@suda.edu.cn (Y. Liu), zhkang@suda.edu.cn (Z. Kang).

method is the introduction of sacrificial agents (commonly used S^{2-}/SO_3^{2-} , formic acid, and lactic acid), which consumes the photo induced holes so as to stabilize the catalysts as well as release a large amount of hydrogen [29–31]. Another way to stabilize and enhance the photocatalytic property of CdS is the important role played by cocatalyst (usually noble metals), which is a kind of materials that can provide either reduction or oxidation active sites, lower the activation energies for surface reaction, accelerate the consumption of holes to reduce photocorrosion and improve the separation efficiency of photogenerated electron-hole pairs [32,33]. Last but not least, the design and fabrication of heterostructured CdS composite catalysts with coordinated band structures, high electron-hole separation and transportation efficiency also provides a feasible solution [34,35]. An efficient and stable CdS system that produce hydrogen and oxygen without the requirement of any sacrificial agents or cocatalysts is still under construction.

Carbon nanodots (CDs) are one of burgeoning carbon nanomaterials (graphite-like particles) with mono-dispersion and small size, usually less than 10 nm in diameter [36]. The CDs with advantages of functional surface moieties, unique electron reservoir, photo-induced electron transfer property, stability, and high specific surface area have been widely applied in photocatalysis [37–39]. The active edges of CDs are often anchored with different kinds of functional moieties, such as $-COOH$, $-OH$, and $C=O$, which play vital important role in the applications. Up to now, a lot of studies have focused on the CDs acting as a very good catalyst for photocatalytic solar water splitting. The incorporation of CDs in photocatalysts can enhance the absorbance of light and electron transfer and decomposition of photo induced electron-hole pairs, hence improve the photocatalytic property of catalysts.

Here, we report a nanocomposite composed of CdS nanosheets loaded with ~ 5 nm sized CDs particles. When the CDs concentration of the sample is $0.03 \text{ g}_{CDs}/\text{g}_{catalyst}$ (the optimum condition), the synthesized heterostructure exhibits excellent hydrogen evolution property ($2.55 \mu\text{mol h}^{-1}$) and low O_2 production ($0.52 \mu\text{mol h}^{-1}$) without any requirement of sacrificial agents or cocatalysts compared to the commonly reported CdS catalysts. It is also notable that our catalyst exhibits excellent stability for about 8-time repetitive experiments, for each time is 12 h visible light irradiation ($\lambda \geq 420 \text{ nm}$). One interesting thing is that when we further increase the concentration of CDs in the composite, the stoichiometric ratio of generated H_2 and O_2 gradually change to 2:1, even the H_2 production is very low. However, the pure CdS nanosheets produce little quantity of H_2 , and show serious photocorrosion within short time.

2. Experimental section

2.1. Synthesis of photocatalyst

2.1.1. Synthesis of CDs

CDs were produced by a typical electrolytic method, with two graphite rods as carbon sources [40]. In particular, two 99.99% pure graphite rods with diameter of 6.15 mm and length of 15 cm (from Alfa Aesar Co. Ltd.) were cleaned in deionized water by ultrasonic agitation for 15 min for 3 times. Then cleaned rods were utilized as anode and cathode respectively in an electrolytic bath of ultrapure water ($18.5 \text{ M}\Omega \text{ cm}^{-1}$, 1000 mL). The two electrodes were set apart of each other with a distance of 7 cm, and protruded 5 cm above the electrolyte level. Then, 30 V was applied across the electrodes using a direct current (DC) power supply. The electrolytic process was running for ten days under intense magnetic stirring. The originally colorless electrolyte changed from a light to a dark solution gradually through the long process. The solution containing CDs was then filtered with a slow-speed quantitative filter paper, and

the resultant solution was centrifuged at 8000 rpm for 30 min to remove the precipitated graphite oxide and big graphite particles. Then the CDs powder was obtained by freeze drying.

2.1.2. Synthesis of CdS nanosheets

The CdS nanosheets were synthesized by a solvothermal method which has been reported more than once [41]. Typically, 0.3206 g of sulfur powder and 0.3654 g of $\text{CdCl}_2 \cdot 2.5\text{H}_2\text{O}$ were dissolved in 60 mL diethylenetriamine (DETA) and stirred for 1 h to get a homogeneous solution. Then, the mixture was transferred into a 100 mL Teflon-lined stainless-steel autoclave, and kept at 80°C for 72 h. After cooling to room temperature, a yellow product was collected by centrifugation. Then the product was washed by ethanol and distilled water respectively for several times. Finally, the samples were dried at 60°C in a vacuum drying oven to get the luminous yellow powder.

2.1.3. Synthesis of CDs-CdS nanocomposite

The synthetic process of CDs-CdS nanocomposite was similar to that of CdS in the following procedure: 0.3206 g of sulfur powder and 0.3654 g of $\text{CdCl}_2 \cdot 2.5\text{H}_2\text{O}$ were dissolved in 60 mL DETA, then different quantity of CDs (0.001, 0.005, 0.01, 0.02, and 0.03 g) were added into the mixture, respectively. Ultrasonic dispersion was required for at least 30 min to get a homogeneous solution. After that, the hydrothermal treatment and washing process was the same with that of the pure CdS. The only difference was that the colours of CDs-CdS samples changed from yellow to dark yellow with the increasing quantity of CDs.

2.2. Characterization

All the reagents are purchased from Sigma and Alfa Aesar without further purification. Transmission electron microscopy (TEM), high-resolution transmission electron microscopy (HRTEM) and energy dispersive x-ray analysis (EDAX) were measured by using a FEI-Tecna F20 transmission electron microscope with an accelerating voltage of 200 kV. The size distribution was measured by dynamic light scattering (DLS) on a Malvern ZEN3690. The scanning electron microscope (SEM) and energy dispersive spectrometer (EDS) function were both applied to characterize the surface morphology and element contents of the samples. The fourier transform infrared (FTIR) spectrum of the samples was acquired from a Hyperion spectrophotometer (Bruker) at the scan range of $400\text{--}4000 \text{ cm}^{-1}$. UV/VIS/NIR spectrophotometer (Lambda 750, Perkinelmer) was employed to acquire the UV-vis absorption spectra. Raman spectra were collected by using a HR 800 Raman spectroscope (J Y, France) with a 20 mW air-cooled argon ion laser (633 nm) as the excitation source. Powder X-ray diffraction (XRD) was carried out to characterize the crystal structure of the as-prepared products by using a PIXcel3D X-ray diffractometer (Empyrean, Holland Panalytical) with $\text{Cu K}\alpha$ radiation ($\lambda = 0.154178 \text{ nm}$). X-ray photoelectron spectroscopy (XPS) measurements were conducted on a KRATOS Axis ultra-DLD X-ray photo-electron spectroscope with a monochromatic $\text{Mg K}\alpha$ X-ray source ($h\nu = 1283.3 \text{ eV}$). Ultraviolet photoelectron spectroscopy (UPS) measurements were performed with He I (21.22 eV) as the monochromatic light source and a total instrumental energy resolution of 100 meV. All the electrochemical measurements were conducted on a CHI 920C workstation (CH Instruments, Shanghai, China), using a standard three-electrode system, of which a platinum wire is used as the reference electrode, a saturated calomel electrode (SCE) as the counter electrode and a glass carbon (GC) electrode as working electrode. The photoresponse-time curves were obtained at open circuit potential (OCP) in 0.1 M sodium sulphate (Na_2SO_4) with a 300 W Xe-lamp as the light source. Electrochemical impedance spectra (EIS) measurements were carried

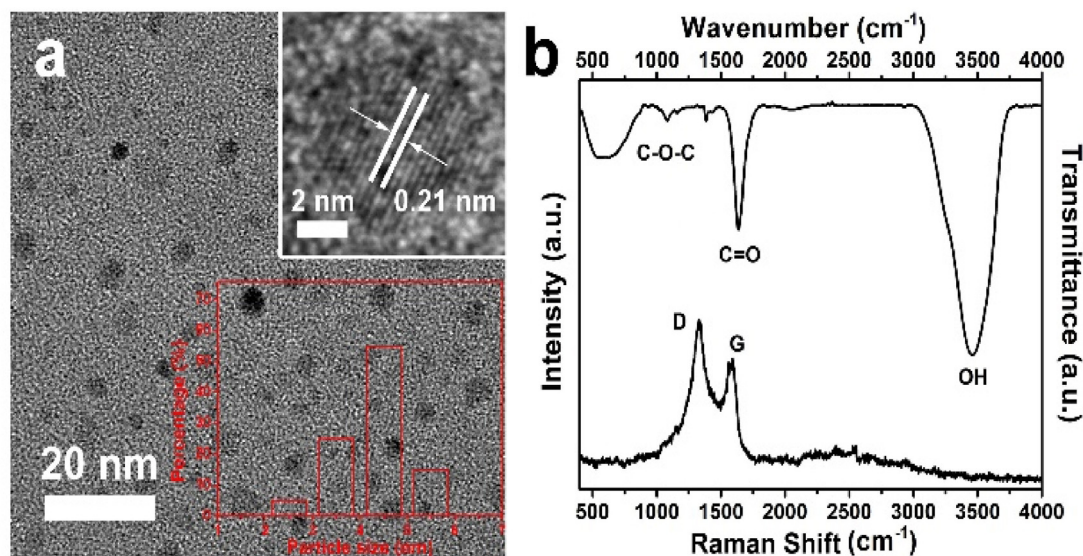


Fig. 1. (a) Typical TEM image of mono-dispersed CDs particles, where the insets are HRTEM image and size distribution, respectively. (b) Raman and FTIR spectra of CDs.

out at open circuit potential as well, with a frequency range from 1 MHz to 0.01 Hz and an AC voltage amplitude of 5 mV in ultrapure water. A Horiba Jobin Yvon (Fluoro Max-4) luminescence spectrometer was employed to record the photoluminescence (PL) spectra.

2.3. Water splitting test

The photocatalytic property of the as-prepared samples was evaluated using (300 W Xe-lamp, PLS-SXE 300, Beijing Trustech Co. Ltd, China), a bandpass filter was used to get visible light ($\lambda \geq 420$ nm). No sacrificial or cocatalysts were needed. In a typical process, 50 mg of the as-prepared sample was added into 25 mL ultrapure water, and ultrasonic dispersion was carried out for at least 30 min to get a homogenous solution. Then the homogenous solution was transferred to a Pyrex glass photoreactor (equipped with a flat window at the top for illumination, and a magneton at the bottom), which was connected to a closed gas-circulation system. Afterwards, the system was degassed to completely remove air (including dissolved air). The temperature of the mixed liquor was maintained at 25 °C by cyclic water installation during the photocatalytic reaction. To detect the gas production, a gas chromatograph (GC-7900) set up with a 5 Å molecular sieves column and a thermal conductivity detector (TCD) was utilized. During the measurement, the temperature parameters of oven, injection and detector were set as 80, 100, and 120 °C, respectively. Argon (Ar) was used as the carrier gas with the flow rate of 30 mL min⁻¹.

2.4. Hydrogen peroxide (H₂O₂) generation test

To detect whether H₂O₂ was formed during the photocatalytic water splitting process. The liquid supernatant was detected by UV–vis spectroscopy using *o*-tolidine as the peroxide indicator [38,39]. By centrifugalizing the catalyst suspension at 8000 rpm for 10 min, 3 mL of liquid supernatant was collected, and then 1 mL 1% *o*-tolidine in 0.1 M HCl was added. Finally, UV–vis absorption spectrum was used to characterize whether the mixture has a maximum peak at 436 nm, which is the typical peak generated by H₂O₂.

2.5. Determination of electron transfer number

The electron transfer number was determined via rotating disk-ring electrodes (RRDE) testing system (RRDE-3A, ALS Co., Ltd). RRDE

experiments were carried out in ultrapure water (N₂ saturated) with a scan rate of 10 mV s⁻¹ and a rotating speed of 1600 rpm. The disk potential was set at open circuit potential avoid electrochemical catalysis process for water oxidation. The ring potential was kept at 0.9 V vs. SCE, which can oxidize the generated H₂O₂ on the disk to O₂. All the process and data were recorded by a CHI 920C electrochemical workstation (CH Instruments, Shanghai, China).

The electron transfer number (*n*) was evaluated according to the following equation [38,39]:

$$n = \frac{4I_d}{I_d + I_r/N}$$

In the formula, *I_d* and *I_r* represent the disk and ring current, respectively, while *N* is the RRDE collection efficiency determined to be 0.24.

3. Results and discussion

3.1. Characterization of CDs and photocatalysts

The TEM and high-resolution TEM images taken from free CDs are given in Fig. 1a, which show spherical and uniformly distributed carbon particles (2–6 nm in diameter measured by DLS) with a lattice spacing of 0.21 nm, corresponding to the (100) lattice planes spacing of graphitic carbon. The Raman spectrum of CDs (Fig. 1b) shows two prominent peaks centred at around 1325 and 1584 cm⁻¹, which are ascribed to the D band of the presence of sp³ defects, and G band due to in-plane vibration of sp² carbon. The functional groups measured by FTIR spectrum is also provided in Fig. 1b, where the peaks located at 3446, 1635 and 1100 cm⁻¹ are assigned to the stretching vibration of OH, C=O, and C–O–C, respectively [42].

The CDs–CdS nanocomposites synthesized using hydrothermal treatment exhibit excellent photocatalytic property and good stability in water splitting. Characterization of the as-prepared CDs–CdS nanocomposite by TEM is displayed in Fig. 2a, showing stacked sheet-like structure. The HRTEM image is shown in Fig. 2b, where the lattice spacing of 0.21 nm shows great correspondence to free CDs (CD is highlighted in a red dashed circle). While the 0.33 nm corresponds to the (002) spacing of CdS [24,41], consistent with the pure phase CdS observed in Fig. S1. The corresponding EDAX images shown in Fig. 2c exhibit uniformly distributed elements of

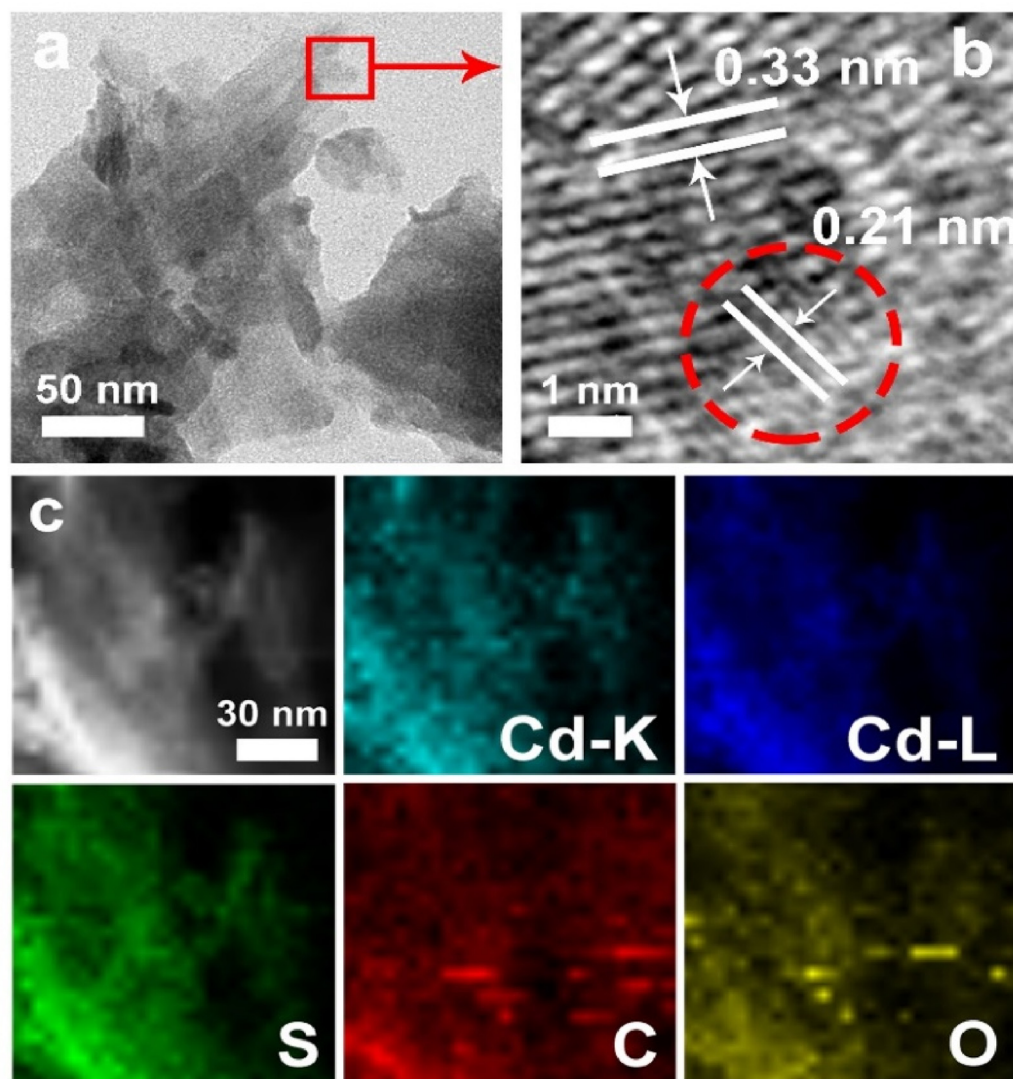


Fig. 2. (a) Typical TEM image, (b) HRTEM image, and (c) EDS of CDs-CdS nanocomposites. Here, for all the CDs-CdS sample measured, the CDs concentration is $0.03 \text{ g}_{\text{CDs}}/\text{g}_{\text{catalyst}}$.

S, Cd, C, and O in the sample. The SEM images presented in Fig. S2 denote the stacked sheet-like morphology of CdS and CDs-CdS, demonstrating that the incorporation of CDs makes no change to the morphology of nanosheets. The EDS spectra (Fig. S3) offer element compositions of CdS and CDs-CdS samples. The atomic ratio of Cd and S is approximately 1, also indicating that the obtained CdS nanosheets are pure phase (Fig. S3). All the results above reveal that the CDs-CdS nanocomposite consists of sheet-like CdS and loaded CDs, and the CDs have a good combination with CdS.

The XRD patterns from the pure CDs, pure CdS, and CDs-CdS are provided in Fig. 3a, where the peaks of CdS and CDs-CdS are consistent with the hexagonal phase CdS (JCPDS 41-1049) [19,24,41], revealing that the adding of CDs doesn't change the molding of CdS nanosheets. It is noted that the XRD peaks of CDs are not observed in CDs-CdS, due to the overlap with CdS peaks. The XPS was also measured to analyze the element composition of the CDs-CdS composites. The core level S 2p spectrum is shown in Fig. 3b, which can be fitted into two individual peaks S 2p_{3/2} and S 2p_{1/2} at 160.3 and 161.4 eV, with a splitting energy of 1.1 eV, corresponding to the valence state of S²⁻ in CdS [43–45]. The deconvoluted peaks of the Cd 3d_{5/2} and Cd 3d_{3/2} located at 403.9 and 410.6 eV with a splitting energy of 6.7 eV finely indicate the Cd²⁺ in CdS (Fig. 3c) [43–45].

The C 1s high resolution spectrum comes from the CDs loaded on the CdS nanosheets, where the peak at 284.6 eV is assigned to the C–C/C=C of the graphite structure of CDs, while the binding energy at 286.3 and 288.2 eV can be attributed to the C–O and C=O bond, respectively [40,42,46]. The survey spectrum of CDs-CdS composite is provided in Fig. S4, showing no peaks of other elements except for C, O, Cd, and S. As a comparison, the XPS spectra of the pure CdS nanosheet were also measured as shown in Fig. S5, exhibiting no signal for C. The XPS spectra also demonstrate that the CDs are tightly combined with CdS nanosheet in CDs-CdS composites. Therefore CDs-CdS possesses higher charge carrier transfer capability than pure CdS.

3.2. Band structure of CDs-CdS

As indicated in Fig. 4a, the incorporation of CDs on the CdS nanosheets dramatically increased the light absorption over the whole detected wavelength range of the UV–vis absorption spectrum. The optical band gap of a semiconductor with great importance can be estimated from the Tauc plot, which is derived

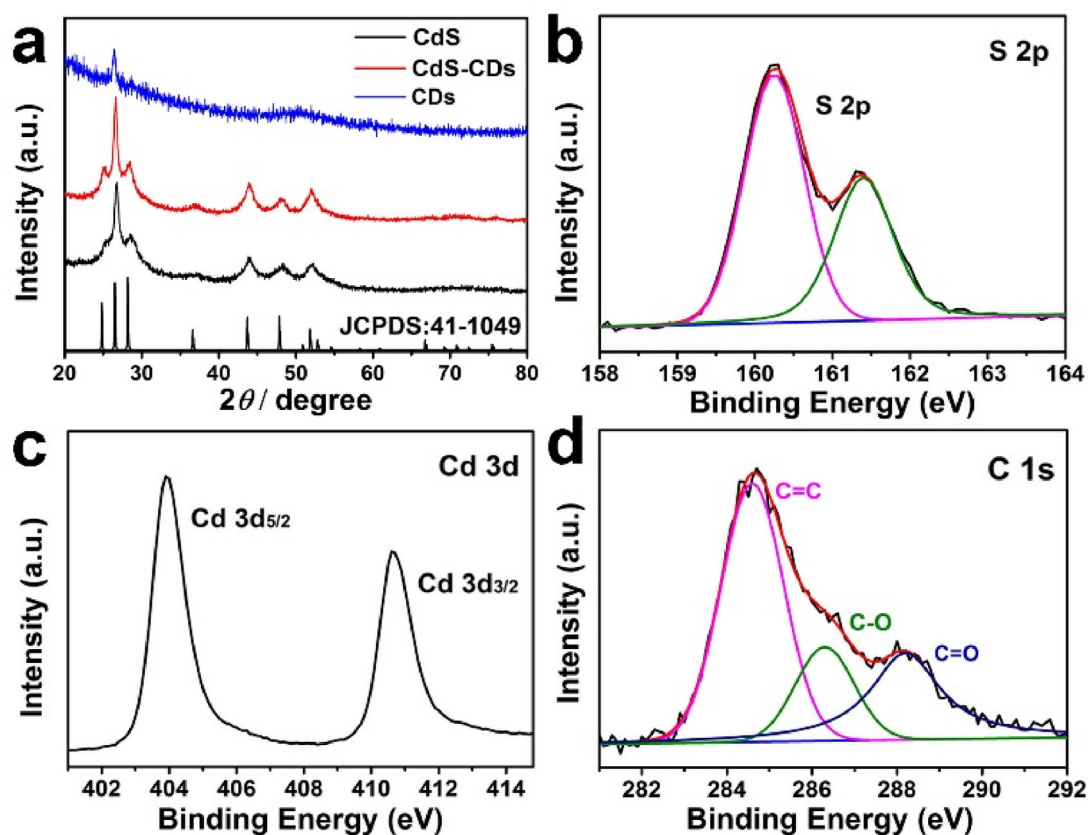


Fig. 3. (a) XRD patterns of CdS (black), CDs (blue) and CDs-CdS (red). XPS spectra of CDs-CdS of (b) S 2p, (c) Cd 3d, and (d) C 1s. All the CDs-CdS has the same CDs concentration of 0.03 g_{CDs}/g_{catalyst}. (For interpretation of the references to colour in this figure legend, the reader is referred to the web version of this article.)

from the UV–vis absorption spectrum. The calculation is based on the following equation [38,39]:

$$\alpha = A(h\nu - E_g)^{n/2} / h\nu$$

In the formula, the parameters α , A , h , ν and E_g correspond to the absorption coefficient, proportionality constant, Planck's constant, frequency of the incident light and band energy, respectively (n in the index is equal to 1 here for direct band gap). The switched Tauc plots of the $(\alpha h\nu)^2$ versus photon energy ($h\nu$) are displayed in Fig. 3b, where the two intersections of the tangent lines and the baseline denote the band gap energies. Thus, the band gap energy (E_g) of the CDs-CdS is determined to be 2.2 eV by identifying the intersection, which is slightly smaller than that of synthesized pure CdS (Fig. 4b black line, 2.31 eV), indicating an easier trend for CDs-CdS to generate the electron-hole pairs by absorbing wider wavelength of light. For water splitting, a photocatalyst needs an appropriate band gap standing for a good match between the CB, VB levels and the redox potentials of the photocatalytic reactions. Therefore, UPS (Fig. 4c) is employed to identify the ionization potential (equivalent to the valence band energy E_v) of CDs-CdS. By subtracting the width of the He I UPS spectrum from the exciting energy (21.22 eV), the E_v is calculated to be 6.52 eV, and E_c is determined to be 4.12 eV ($E_c = E_v - E_g$). To well define the correspondence of the CB and VB levels towards the redox potentials, electron volts are converted to electrochemical energy potentials in volts with reference to the reference standard (versus reversible hydrogen electrode (RHE)), where 0 V is equal to -4.44 eV versus E_{vac} (vacuum level). Fig. 4d shows the integration of band energy and redox potentials in the same coordinate, which demonstrates that the CB level of CDs-CdS is positioned above the reduction level for H_2 , and the VB level is located below the oxidation level for

H_2O to H_2O_2 or O_2 . The correspondence of the band energy and redox potentials allows induced electrons and holes to transfer and react with H_2O molecules, thus confirming CDs-CdS as a potential photocatalyst for water splitting.

3.3. Photocatalytic properties of CDs-CdS

Fig. 5a exhibits the evolution of H_2 and O_2 of optimized CDs-CdS composite (0.03 g_{CDs}/g_{catalyst}) under visible light irradiation ($\lambda \geq 420$ nm) without any sacrificial agents or cocatalysts. H_2 and O_2 were both quantified by gas chromatography (GC). The maximum H_2 production rate was calculated to be $2.55 \mu\text{mol h}^{-1}$, however, the O_2 production is very low ($0.52 \mu\text{mol h}^{-1}$) compared to H_2 (stoichiometry ratio of H_2 and O_2 was about 5:1), demonstrating that the photocorrosion is partly restrained when introducing CDs into CdS. To determine the stability of CDs-CdS, the cyclic stability experiments were carried out (Fig. 4b), which exhibited favourable stability for a catalyst dried and reused for 8 times (for each time is 12 h visible light irradiation ($\lambda \geq 420$ nm)). For the 8th time of the cyclic stability experiment, CDs-CdS perform a H_2 production rate with a loss of 10% compared to the first time. XPS spectra were used to characterize the catalyst after absolute deterioration. As is shown in Fig. S6, the deteriorated sample shows same elements with fresh CDs-CdS, but have different high-resolution spectra. For example, in C 1s spectrum, C–S bond appears which is absent in pristine sample [47]. S 2p spectrum is absolutely different from the pristine with three peaks attributed to S, SO_3^{2-} and SO_4^{2-} , showing that CdS has already thoroughly deteriorated [27,48]. It is notable that Cd spectrum is also totally changed, which is hard to find a correlation. Based on the XPS of the deteriorated sample, it is proposed that during the photocatalytic process, CDs will help to stable

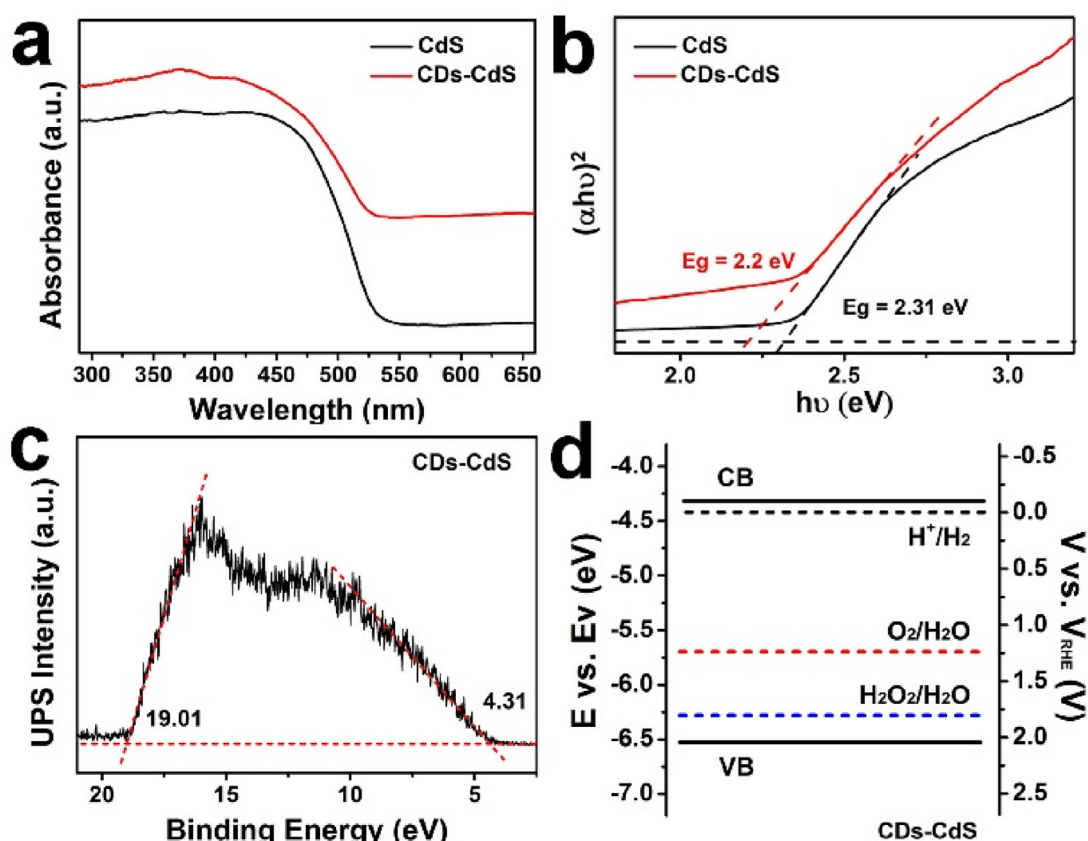


Fig. 4. (a) UV-vis absorption spectra of CdS (black curve) and CDs-CdS (red curve). (b) $(\alpha h\nu)^2$ versus $h\nu$ curve of CdS (black curve) and CDs-CdS (red curve). (c) UPS spectra of CDs-CdS. The horizontal dotted line red lines mark the baseline and the tangents of the curve, where the intersections of the tangents and the baseline show the edges of the UPS spectra, hence determining the UPS width. (d) Band structure diagram for CDs-CdS. VB, valence band; CB, conduction band. For all the samples used, the CDs concentration is 0.03 $g_{CDs}/g_{catalyst}$. (For interpretation of the references to colour in this figure legend, the reader is referred to the web version of this article.)

CdS by suppress the oxidation of CdS by holes, but will gradually react with CdS and form C–S bond after a long time tolerance to the oxidation species, in addition, part of CdS will still undergo the photocorrosion process that always mentioned.

To further explore the influence of CDs on CdS, a series of photocatalytic experiments by adjusting the concentration of CDs in the composites (Fig. 5c) were carried out. For pure CdS with the same synthesis process, a low amount of H_2 was detected after the same photo irradiation, and no oxygen is detected, demonstrating that the CdS were completely photocorroded in short time. For CDs-CdS, it turns out that, the H_2 production is markedly enhanced and reaches the highest value when CDs concentration increases from 0 to 0.03 ($g_{CDs}/g_{catalyst}$), along with a slight increase of O_2 production. We attribute this improvement to the CDs ability to enhance light absorbance and promote the separation and diffusion of charge carriers. Besides, CDs can also promote the production of O_2 by reducing the combination between holes and S^{2-} to stabilize the catalysts. However, for pure CdS, the photo induced holes were consumed by CdS rather than H_2O , hence lost activity very quickly. Unfortunately, excessive CDs seem to occupy the active center on the surface of CdS and obstruct CdS to absorb light, leading to very low H_2 ($0.13 \mu\text{mol h}^{-1}$) and O_2 ($0.06 \mu\text{mol h}^{-1}$) production. The only advantage it brings is that the stoichiometry ratio of generated H_2 and O_2 is finally to be 2:1 and the stability is still maintained. The time-current (i-t) curves for CDs-CdS and CdS were also recorded to estimate the photoresponse properties. As is shown in Fig. 5d, CDs-CdS exhibits a larger photocurrent compared to CdS under the same irradiation, which manifest the facts that, 1) CDs have a strong contact with CdS nanosheets which is very crucial for a fast charge

transport speed and high separation efficiency; 2) CDs-CdS shows gradually decrease of photocurrent while that of CdS appears an apparent decay trend, demonstrating that CDs-CdS has a strong resistance against photocorrosion.

3.4. Study on the photocatalytic mechanism and process

The EIS was carried out to further confirm that the CDs-CdS has a better ability to transfer generated charge carriers (Fig. 6a). A smaller semicircle in the EIS Nyquist plot is recognized to indicate a faster interfacial electron transfer speed [49]. It can be easily observed that CDs-CdS has a smaller semicircle than pure CdS, demonstrating that CDs loading on CdS nanosheets serve an effective separation of photogenerated charge carriers due to the strong interaction between CDs and CdS. PL spectra for CdS, and CDs-CdS shown in Fig. 6b were recorded with an excitation wavelength of 340 nm, respectively, where CDs-CdS exhibits a weaker and narrower emission in the range of 400–600 nm than CdS, demonstrating that the photogenerated charge carriers were transferred from CdS to CDs in CDs-CdS nanocomposites. Another conclusion derived from the attenuated PL signal is a higher separation efficiency for CDs-CdS, which is also very important in photocatalytic water splitting [50]. The electron transfer number (n) of CDs-CdS was determined via the RRDE curves displayed in Fig. 6c, where n is calculated to be 3.1, consisting of both 2/4-electron process. Above demonstrates that CDs-CdS has met the basic condition to produce both H_2O_2 and O_2 . However, from Fig. 6d, no obvious signal of H_2O_2 was detected for CDs-CdS, which seems that CDs-CdS produce trace amount of H_2O_2 during the photocatalytic process,

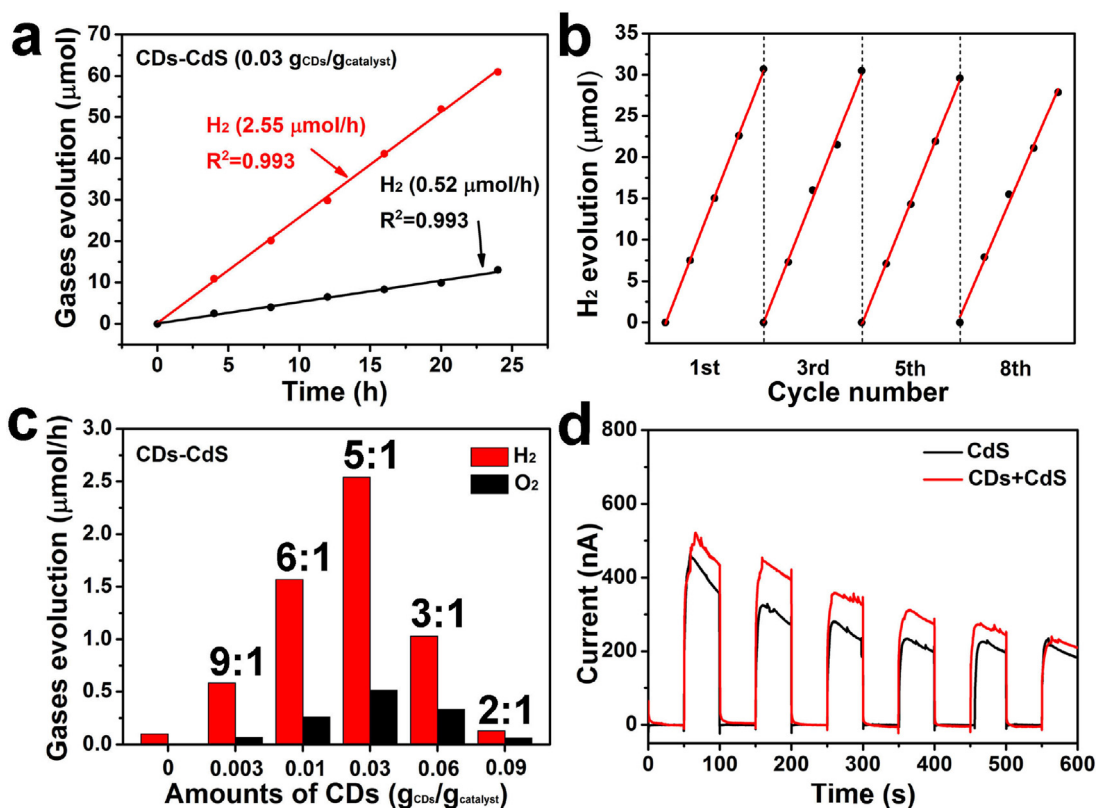


Fig. 5. (a) Dependence of evolution of H₂ and O₂ from water on time course under visible light irradiation ($\lambda \geq 420$ nm), catalysed by CDs-CdS (0.03 g_{CDs}/g_{catalyst}). (b) The cyclic stability of CDs-CdS (0.03 g_{CDs}/g_{catalyst}) for photocatalytic water splitting under visible light. (c) Amount of gases evolution of CDs-CdS with different quantity of CDs. (d) Photoresponse curves of CdS and CDs-CdS (0.03 g_{CDs}/g_{catalyst}). All the ratios above the bar charts represent the stoichiometric ratio of generated H₂ and O₂.

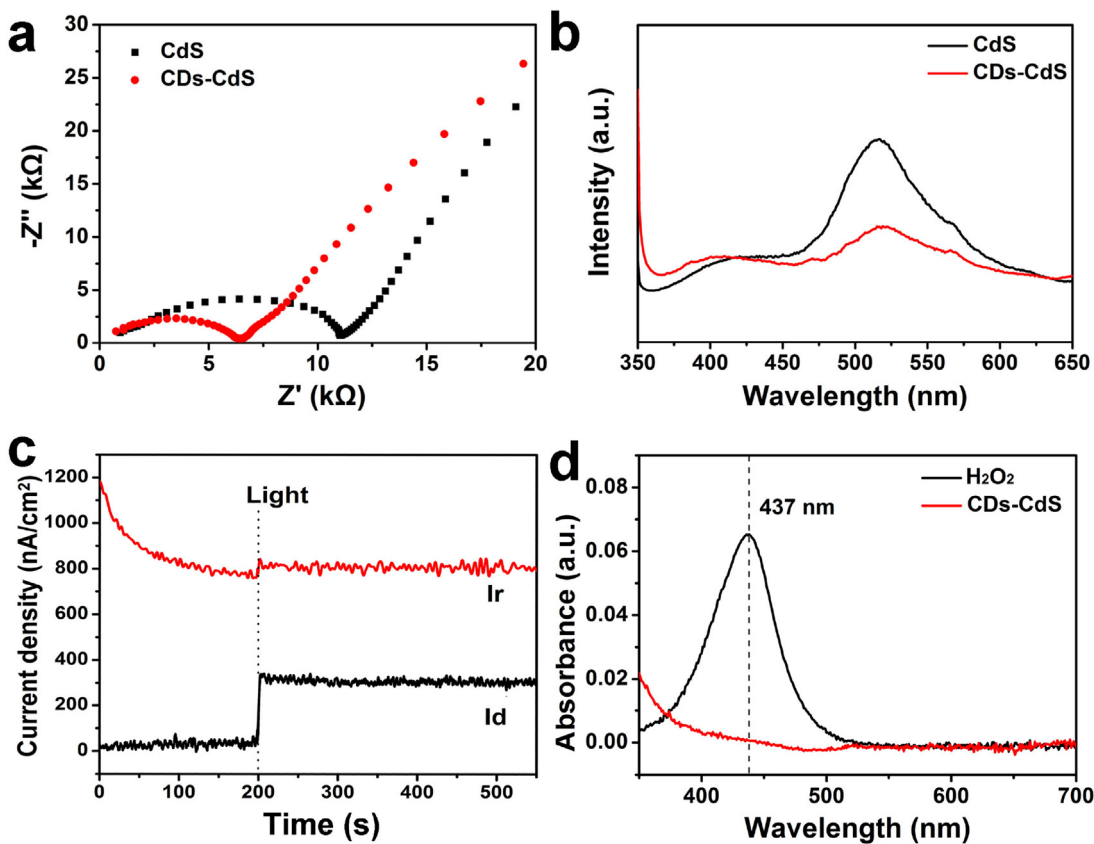


Fig. 6. (a) EIS curves of CdS and CDs-CdS. (b) PL spectra of CdS and CDs-CdS with an excitation wavelength of 340 nm. (c) RRDE i-t curves of CDs-CdS under dark or light. (d) UV-vis absorbance spectra of H₂O₂ calibration curve and tested curve for CDs-CdS. Here, all the CDs-CdS samples have the same CDs concentration of 0.03 g_{CDs}/g_{catalyst}.

while O_2 is produced via 4-electron pathway, with part of the holes combining with CdS. This result also explains why CDs-CdS produce little quantity of O_2 , and less H_2 evolution gradually on account of delayed photocorrosion.

Based on all the results above, a plausible mechanism for the CDs-CdS nanocomposites in photocatalytic water splitting under visible light was proposed. The CdS nanosheets with an appropriate band gap can easily absorb visible light ($\lambda \geq 420$ nm) and generate the photo-induced electron-hole pairs. In general, part of the charge carriers will recombine with each other hence annihilate quickly. However, for CDs-CdS nanocomposites, these charge carriers generated on CdS will transfer to CDs due to a strong interaction between CDs and CdS nanosheets, leading to a rapid separation of the electron-hole pairs. Besides, CDs loaded on CdS nanosheets enhance the absorption towards visible light, resulting in a higher utilization ratio of energy. More importantly, the electron-hole pairs transferred to CDs can react with H_2O instead of CdS itself, especially the holes, hence making CDs-CdS a stable photocatalyst for water splitting without requirement for any sacrificial agents.

4. Conclusion

CDs-CdS nanocomposites synthesized by hydrothermal treatment were introduced as a photocatalyst for visible light water splitting without requirement for any sacrificial agents. The CDs-CdS nanocomposite with a CDs concentration of $0.03 \text{ g}_{\text{CDs}}/\text{g}_{\text{catalyst}}$ exhibits the highest H_2 production for about $2.55 \mu\text{mol h}^{-1}$, and the O_2 production of $0.52 \mu\text{mol h}^{-1}$ with outstanding stability for about 8-time cyclic experiments. The only shortcoming for this efficient catalysts is that the stoichiometric ratio of generated H_2 and O_2 do not equal to 2:1, leading to the consequence that CdS in CDs-CdS will eventually be photocorroded. By controlling the CDs concentration in the catalysts, we finally achieved the stoichiometric ratio of 2:1 of generated H_2 and O_2 , however the gases production are very low in this situation. Even our results have shortcoming, it is still the first time to realize stable photocatalytic water splitting for CdS without sacrificial agents, which opens a new door for the development of CdS catalysts.

Acknowledgments

This work is supported by Collaborative Innovation Center of Suzhou Nano Science and Technology, the National Natural Science Foundation of China (51422207, 51572179, 21471106, 21501126), the Natural Science Foundation of Jiangsu Province (BK20161216) and a project funded by the Priority Academic Program Development of Jiangsu Higher Education Institutions (PAPD).

Appendix A. Supplementary data

Supplementary data associated with this article can be found, in the online version, at <http://dx.doi.org/10.1016/j.apcatb.2017.05.049>.

References

- [1] A. Kudo, Y. Miseki, *Chem. Soc. Rev.* 38 (2009) 253–278.
- [2] Y. Ma, X. Wang, Y. Jia, X. Chen, H. Han, C. Li, *Chem. Rev.* 114 (2014) 9987–10043.
- [3] X.C. Wang, K. Maeda, A. Thomas, K. Takanabe, G. Xin, J.M. Carlsson, K. Domen, M. Antonietti, *Nat. Mater.* 8 (2009) 76–80.
- [4] N.Z. Muradov, T.N. Veziroglu, *Int. J. Hydrogen Energy* 33 (2008) 6804–6839.
- [5] M.G. Walter, E.L. Warren, J.R. McKone, S.W. Boettcher, Q.X. Mi, E.A. Santori, N.S. Lewis, *Chem. Rev.* 110 (2010) 6446–6473.
- [6] A. Fujishima, K. Honda, *Nature* 238 (1972) 37–38.
- [7] M. Ni, M.K.H. Leung, D.Y.C. Leung, K. Sumathy, *Renew. Sustain. Energy Rev.* 11 (2007) 401–425.
- [8] X.B. Chen, S.H. Shen, L.J. Guo, S.S. Mao, *Chem. Rev.* 110 (2010) 6503–6570.
- [9] Y. Bai, I. Mora-Seró, F. De Angelis, J. Bisquert, P. Wang, *Chem. Rev.* 114 (2014) 10095–10130.
- [10] B.A. Pinaud, J.D. Benck, L.C. Seitz, A.J. Forman, Z.B. Chen, T.G. Deutsch, B.D. James, K.N. Baum, G.N. Baum, S. Ardo, H.L. Wang, E. Miller, T.F. Jaramillo, *Energy Environ. Sci.* 6 (2013) 1983–2002.
- [11] T. Hisatomi, J. Kubota, K. Domen, *Chem. Soc. Rev.* 43 (2014) 7520–7535.
- [12] K. Maeda, K. Domen, *J. Phys. Chem. Lett.* 1 (2010) 2655–2661.
- [13] H.J. Li, W.G. Tu, Y. Zhou, Z.G. Zou, *Adv. Sci.* 3 (2016) 1500389.
- [14] H.Q. Li, X. Wang, J.Q. Xu, Q. Zhang, Y. Bando, D. Golberg, Ying Ma, T.Y. Zhai, *Adv. Mater.* 25 (2013) 3017–3037.
- [15] L. Huang, J.H. Yang, X.L. Wang, J.F. Han, H.X. Han, C. Li, *Phys. Chem. Chem. Phys.* 15 (2013) 553–560.
- [16] Y.X. Li, Y.F. Hu, S.Q. Peng, G.X. Lu, S.B. Li, *J. Phys. Chem. C* 113 (2009) 9352–9358.
- [17] N.Z. Bao, L.M. Shen, T. Takata, D.L. Lu, K. Domen, *Chem. Lett.* 35 (2006) 318–319.
- [18] Q. Li, B.D. Guo, J.G. Yu, J.R. Ran, B.H. Zhang, H.J. Yan, J.R. Gong, *J. Am. Chem. Soc.* 133 (2011) 10878–10884.
- [19] Y. Xu, W.W. Zhao, R. Xu, Y.M. Shi, B. Zhang, *Chem. Commun.* 49 (2013) 9803–9805.
- [20] M. Sathish, B. Viswanathan, R.P. Viswanath, *Int. J. Hydrogen Energy* 31 (2006) 891–898.
- [21] J. Fang, L. Xu, Z. Zhang, Y. Yuan, S. Cao, Z. Wang, L. Yin, Y. Liao, C. Xue, *ACS Appl. Mater. Interfaces* 5 (2013) 8088–8092.
- [22] I. Robel, B.A. Bunker, P.V. Kamat, *Adv. Mater.* 17 (2005) 2458–2463.
- [23] L. Jia, D.H. Wang, Y.X. Huang, A.W. Xu, H.Q. Yu, *J. Phys. Chem. C* 115 (2011) 11466–11473.
- [24] J.G. Yu, Y.F. Yu, P. Zhou, W. Xiao, B. Cheng, *Appl. Catal. B: Environ.* 156–157 (2014) 184–191.
- [25] J.F. Reber, M. Rusek, *J. Phys. Chem.* 90 (1986) 824–834.
- [26] J. Xian, D. Li, J. Chen, X. Li, M. He, Y. Shao, L. Yu, J. Fang, *ACS Appl. Mater. Interfaces* 6 (2014) 13157–13166.
- [27] D. Meissner, C. Benndorf, R. Memming, *Appl. Surf. Sci.* 27 (1987) 423–436.
- [28] Y.H. Tang, X. Hua, C.B. Liu, *Phys. Chem. Chem. Phys.* 16 (2014) 25321–25329.
- [29] N.Z. Bao, L.M. Shen, T. Takata, K. Domen, *Chem. Mater.* 20 (2008) 110–117.
- [30] X. Zong, H.J. Yan, G.P. Wu, G.J. Ma, F.Y. Wen, L. Wang, C. Li, *J. Am. Chem. Soc.* 130 (2008) 7176–7177.
- [31] K. Chang, M. Li, T. Wang, S.X. Ouyang, P. Li, L.Q. Liu, J.H. Ye, *Adv. Energy Mater.* 5 (2015) 1402279.
- [32] J.H. Yang, D. Wang, H.X. Han, C. Li, *Acc. Chem. Res.* 46 (2013) 1900–1909.
- [33] X. Zong, J.F. Han, G.J. Ma, H.J. Yan, G.P. Wu, L. Can, *J. Phys. Chem. C* 115 (2011) 12202–12208.
- [34] H.J. Li, Y. Zhou, W.G. Tu, J.H. Ye, Z.G. Zou, *Adv. Funct. Mater.* 25 (2015) 998–1013.
- [35] X.W. Wang, G. Liu, Z.G. Chen, F. Li, L.Z. Wang, G.Q. Lu, H.M. Cheng, *Chem. Commun.* 23 (2009) 3452–3454.
- [36] H.T. Li, Z.H. Kang, Y. Liu, S.T. Lee, *J. Mater. Chem.* 22 (2012) 24230–24253.
- [37] H.J. Yu, R. Shi, Y.F. Zhao, G.I.N. Waterhouse, L.Z. Wu, C.H. Tong, T.R. Zhang, *Adv. Mater.* 28 (2016) 9454–9477.
- [38] X.Q. Wu, J. Zhao, S.J. Guo, L.P. Wang, W.L. Shi, H. Huang, Y. Liu, Z.H. Kang, *Nanoscale* 8 (2016) 17314–17321.
- [39] J. Liu, Y. Liu, N.Y. Liu, Y.Z. Han, X. Zhang, H. Huang, Y. Lifshitz, S.T. Lee, J. Zhong, Z.H. Kang, *Science* 347 (2015) 970–974.
- [40] H. Ming, Z. Ma, Y. Liu, K.M. Pan, H. Yu, F. Wang, Z.H. Kang, *Dalton Trans.* 41 (2012) 9526–9531.
- [41] S. Ma, J. Xie, J.Q. Wen, K.L. He, X. Li, W. Liu, X.C. Zhang, *Appl. Surf. Sci.* 391 (2017) 580–591.
- [42] H.T. Li, R.H. Liu, W.Q. Kong, J. Liu, Y. Liu, L. Zhou, X. Zhang, S.T. Lee, Z.H. Kang, *Nanoscale* 6 (2014) 867–873.
- [43] A.H. Ye, W.Q. Fan, Q.H. Zhang, W.P. Deng, Y. Wang, *Catal. Sci. Technol.* 2 (2012) 969–978.
- [44] R.S. Zeng, R.A. Song, Y.Q. Zhao, X.S. Li, Z.G. Sun, Y.Y. Shen, *Nanotechnology* 25 (2014) 135602.
- [45] J.H. Yang, J. Wang, X.Y. Li, D.D. Wang, H. Song, *Catal. Sci. Technol.* 6 (2016) 4525–4534.
- [46] J. Liu, S.Y. Zhao, C.X. Li, M.M. Yang, Y.M. Yang, Y. Liu, Y. Lifshitz, S.T. Lee, Z.H. Kang, *Adv. Energy Mater.* 6 (2016) 1502039.
- [47] Y.Q. Dong, H.C. Pang, H.B. Yang, C.X. Guo, J.W. Shao, Y.W. Chi, C.M. Li, T. Yu, *Angew. Chem. Int. Ed.* 52 (2013) 7800–7804.
- [48] A.G. Schaaf, H.W. Nesbitt, I. Kartio, K. Laajalehto, G.M. Bancroft, R. Szargan, *Surf. Sci.* 411 (1998) 321–328.
- [49] J. Lim, D. Monllor-Satoca, J.S. Jang, S. Lee, W. Choi, *Appl. Catal. B* 152 (2014) 233–240.
- [50] Y. He, L. Zhang, B. Teng, M. Fan, *Environ. Sci. Technol.* 49 (2015) 649–656.